The smart surface modification of Fe_2O_3 by WO_x for significantly promoting the selective catalytic reduction of NO_x with NH_3

Fudong Liu[a,1,2], Wenpo Shan[b,2], Zhihua Lian[b], Jingjing Liu[a,c], Hong He[a,b,c,*]

[a] State Key Joint Laboratory of Environment Simulation and Pollution Control, Research Center for Eco-Environmental Sciences, Chinese Academy of Sciences, Beijing 100085, China
[b] Center for Excellence in Regional Atmospheric Environment, Institute of Urban Environment, Chinese Academy of Sciences, Xiamen 361021, China
[c] University of Chinese Academy of Sciences, Beijing 100049, China

ARTICLE INFO

ABSTRACT

The deposition of WO_x species using conventional impregnation method is a very simple and efficient way to adjust the surface acidity and redox ability of hematite Fe_2O_3 simultaneously, significantly improving its catalytic activity and N_2 selectivity for the selective catalytic reduction of NO_x with NH_3 (NH_3-SCR). The deposited WO_x species on Fe_2O_3 surface was in highly unsaturated coordination state acting as an effective surface modifier. Through the electronic inductive effect in W−O−Fe bonds, the oxidation ability of surface $Fe^{(3+\delta)+}$ species was well increased, yet the over-oxidation of NH_3 on bulk Fe_2O_3 was significantly suppressed, which was quite beneficial to the improvement of NH_3-SCR activity and N_2 selectivity simultaneously. Besides, the deposited WO_x species could also supply abundant surface reactive Lewis and Brønsted acid sites for NH_3 adsorption and activation during the SCR reaction. The NH_3-SCR process on this WO_x/Fe_2O_3 catalyst mainly followed an Eley-Rideal (E-R) reaction pathway between gaseous NO and active NH_3 adsorbed species, which was the main reason for its superior SO_2 resistance. This opens a new route for the preparation of highly efficient, selective, cost effective and SO_2 resistant NH_3-SCR catalysts for the deNO$_x$ process on diesel engines.

1. Introduction

Nitrogen oxides (NO_x, including NO and NO_2) can induce major air pollution problems, such as acid rain, photochemical smog and haze. Great efforts have been devoted to the development and application of NO_x emission control technologies for fossil fuel combustions [1,2]. Due to its high efficiency, excellent selectivity and low cost, selective catalytic reduction of NO_x with NH_3 (NH_3-SCR) has been widely applied for the removal of NO_x from stationary sources since 1970s [3], and this technology has also become the dominant deNO$_x$ technology for diesel vehicles to meet the ever tightened emission standards [4].

Catalysts play a key role in the practical application of NH_3-SCR technology [5,6]. The commercial NH_3-SCR catalyst for stationary source NO_x reduction was mainly WO_3 or MoO_3 doped V_2O_5/TiO_2 [3,7], which was also applied as the first generation NH_3-SCR catalyst on diesel vehicles in Europe. However, the toxicity of active vanadium species, together with high N_2O formation at high temperatures, has restrained its mobile applications [8]. Therefore, great efforts have

been made to develop substitutive, environmentally benign NH_3-SCR catalysts for diesel vehicle emission control. In recent years, some transition metal exchanged zeolites, such as Fe-ZSM-5 [9], and Cu-SSZ-13 [10,11], and vanadium-free oxide catalysts, such as CeO_2-WO_3 oxide [12,13] and CeO_2-TiO_2 oxide [14,15], were developed as potential substitutions for vanadium-based NH_3-SCR catalysts in diesel application.

Iron oxides are environmentally-benign materials which can be used as catalysts for various reactions. The reduction of NO_x with NH_3 can also be catalyzed by Fe-based materials due to their excellent redox ability between Fe^{3+} and Fe^{2+}. The previous studies mainly focused on the shape or morphology-controlled synthesis of Fe_2O_3 [16], the achievement of high dispersion of Fe_2O_3 onto other supports [17] or the synthesis of mixed oxide catalysts with new active phase of Fe species [18]. The developed Fe-based oxide catalysts include γ-Fe_2O_3 nanorods[16], Fe_2O_3-PILC [19], FeTiO$_x$ [18], Fe-Ti spinel [20], Fe_2O_3-SiO_2 aerogel [21], $Fe_2O_3/WO_3/ZrO_2$ [17], and carbon materials supported Fe_2O_3 [22,23]. However, there is barely any report on the surface

modification of Fe_2O_3 to improve its NH_3-SCR performance. The tungsten oxide is usually used as the promoter for NH_3-SCR catalysts to improve the hydrothermal stability or increase the surface acidity [24,25], which has been successfully used to modify CeO_2 for $deNO_x$ process [26]. In this paper, the surface modification effect of WO_x species on Fe_2O_3 will be investigated in detail, supplying a simple and new way to prepare highly efficient NH_3-SCR catalyst for practical use in diesel NO_x reduction.

2. Experimental

2.1. Catalyst preparation

The pristine Fe_2O_3 material was prepared by conventional precipitation method using $Fe(NO_3)_3 \cdot 9H_2O$ as precursor and urea as precipitator. After the dissolution of $Fe(NO_3)_3 \cdot 9H_2O$ into distilled water, excessive urea aqueous solution was added with a urea/Fe molar ratio of 10:1. The mixed solution was then heated to 90 °C and held there for 12 h under vigorous stir. After filtration and washing with distilled water, the resulting precipitate cake was dried at 100 °C for 12 h and subsequently calcined at 500 °C for 3 h in air. The resulting Fe_2O_3 material was then grounded into fine powder for use.

The $\delta\%$ WO_x/Fe_2O_3 catalysts (δ = 1, 5, 10 by weight) were prepared by conventional impregnation method using the above-mentioned Fe_2O_3 as support and $(NH_4)_6H_2W_{12}O_{40} \cdot 5H_2O$ as WO_x precursor. The calculated amount of $(NH_4)_6H_2W_{12}O_{40} \cdot 5H_2O$ precursor was firstly dissolved into distilled water in the presence of $H_2C_2O_4 \cdot 2H_2O$ with equal weight. Then, the Fe_2O_3 powder was added into the solution under vigorous stir. After impregnation, the excess water was removed in a rotary evaporator at 80 °C. The resulting samples were dried at 100 °C for 12 h and finally calcined at 500 °C for 3 h in air. Before NH_3-SCR activity tests, the $\delta\%$ WO_x/Fe_2O_3 power catalysts were pressed into pellets, crushed and sieved to 40–60 mesh. The pristine WO_3 sample was also prepared as reference material by direct decomposition of $(NH_4)_6H_2W_{12}O_{40} \cdot 5H_2O$ in air at 600 °C for 3 h.

2.2. Activity test

The steady state NH_3-SCR and NO/NH_3 oxidation activity over $\delta\%$ WO_x/Fe_2O_3 catalysts (δ = 0, 1, 5, 10) was tested in a fixed-bed quartz tube reactor, and the reaction conditions were controlled as follows: 40–60 mesh catalyst, 500 ppm NO, 500 ppm NH_3, 5 vol.% O_2, 100 ppm SO_2 (when used), 5% H_2O (when used) and N_2 balance; 500 ml/min total flow rate, and catalyst volume of 0.6 mL or 0.3 mL, corresponding to gas hourly space velocity (GHSV) of 50,000 h^{-1} or 100,000 h^{-1}. The effluent gas including NO, NH_3, N_2O and NO_2 was analyzed using an FTIR spectrometer (Nicolet Nexus 670) equipped with a low volume multiple-path gas cell (2 m). The NO_x conversion and N_2 selectivity were calculated according to the formulas described in our previous study [27].

2.3. Characterizations

The N_2 physisorption isotherms were measured at 77 K on Quantachrome Quadrasorb SI-MP. Prior to N_2 physisorption, the samples were degassed at 300 °C for 4 h. Surface areas were determined by BET equation in 0.05–0.35 partial pressure range. Pore volumes and average pore radius were determined by BJH method from desorption and adsorption branches of the isotherms, respectively.

The XRD measurements of $\delta\%$ WO_x/Fe_2O_3 catalysts (δ = 0, 1, 5, 10) were carried out on PANalytical X'Pert Pro Diffractometer with Cu K_α radiation source (λ = 0.15406 nm). The data of 2θ from 10 to 80° were collected at 8°/min with step size of 0.07°.

The *ex situ* XAFS of W-L_{III} edge were measured in fluorescence mode for $\delta\%$ WO_x/Fe_2O_3 catalysts (δ = 1, 5, 10) and in transmission mode for WO_3 reference on BL14W1 beamline, Shanghai Synchrotron Radiation

Facility (SSRF). The *ex situ* XAFS of Fe-K edge in $\delta\%$ WO_x/Fe_2O_3 catalysts (δ = 1, 5, 10) and Fe_2O_3 reference were measured in transmission mode on 1W1B beamline, Beijing Synchrotron Radiation Facility (BSRF). The *in situ* XAFS of Fe-K edge in $\delta\%$ WO_x/Fe_2O_3 catalysts (δ = 1, 5, 10) and Fe_2O_3 reference during the temperature programmed reduction process in 5 vol.% H_2/He from room temperature to 900 °C were measured in transmission mode using quick XAFS (QXAFS) method on BL-12C beamline, Photon Factory, High Energy Accelerator Research Organization (KEK), Japan. XAFS Data were analyzed using the REX2000 program (Rigaku Co.). XANES were normalized with edge height and then taken the first-order derivatives to compare the variation of absorption edge energies. EXAFS oscillation $\chi(k)$ was extracted using spline smoothing with a Cook-Sayers criterion [28], and the filtered k^3-weighted $\chi(k)$ was Fourier transformed into R space in the k range of 2.0–10.5 Å^{-1} for W–L_{III} edge and 2.0–13.0 Å^{-1} for Fe-K edge. In the curve fitting step, the possible backscattering amplitude and phase shift were calculated using FEFF8.4 code [29].

The XPS of $\delta\%$ WO_x/Fe_2O_3 catalysts (δ = 1, 5, 10) and Fe_2O_3, WO_3 references was recorded on Scanning X-ray Microprobe (PHI Quantera, ULVAC-PHI, Inc.) using Al K_α radiation. Binding energies of W 4f, Fe 2p and O 1s were calibrated using C 1s peak (BE = 284.8 eV).

The H_2-TPR experiments of $\delta\%$ WO_x/Fe_2O_3 catalysts (δ = 1, 5, 10) and Fe_2O_3, WO_3 references were carried out on an AutoChem 2920 Chemisorption Analyzer (Micromeritics). The samples with 50 mg weight were pretreated in a quartz tube reactor at 300 °C in a flow of air (50 ml/min) for 1 h and then cooled down to room temperature. Afterwards, the H_2-TPR procedures were performed in a flow of 10 vol. % H_2/Ar (50 ml/min) from room temperature to 1000 °C with the ramping rate of 10 °C/min.

The *in situ* DRIFTS were performed on an FTIR spectrometer (Nicolet Nexus 670) equipped with a smart collector and an MCT/A detector, including the $NH_3/(NO + O_2)$ adsorption over $\delta\%$ WO_x/Fe_2O_3 catalysts (δ = 0, 1, 5, 10) and the transient reactions (*i.e.* reaction between $NO + O_2$ and pre-adsorbed NH_3 species, reaction between NH_3 and pre-adsorbed NO_x species, and reaction in $NH_3 + NO + O_2$ atmosphere) over Fe_2O_3 reference and 5% WO_x/Fe_2O_3 catalyst. The samples were pretreated at 400 °C for 0.5 h in 20 vol.% O_2/N_2 and then cooled down to 200 °C. The background spectra were collected in flowing N_2 and automatically subtracted from the sample spectra. The reaction conditions were controlled as follows: 500 ppm NH_3, 500 ppm NO, 5 vol.% O_2, N_2 balance and 300 ml/min flow rate. For each sample, the $NH_3/(NO + O_2)$ adsorption time was controlled at 1 h. Afterwards, the samples were purged by N_2 for another 0.5 h until the infrared spectroscopy signals were stabilized. Finally, $(NO + O_2)/NH_3$ was introduced into the gas chamber to react with the pre-adsorbed NH_3/NO_x species for 1 h. All spectra were recorded by accumulating 100 scans with 4 cm^{-1} resolution.

3. Results and discussion

3.1. NH_3-SCR activity and the effects of SO_2, H_2O and GHSV

The influence of the deposition amount of WO_x species onto Fe_2O_3 on the NH_3-SCR activity was firstly investigated. As the results shown in Fig. 1, the pristine Fe_2O_3 showed very low NH_3-SCR efficiency with a rather narrow operation temperature window and relatively low N_2 selectivity in the whole temperature range. Only *ca.* 40% NO_x conversion was achieved over the un-promoted Fe_2O_3 at 300 °C. Interestingly, the simple deposition of WO_x species onto Fe_2O_3 surface resulted in a significant enhancement of $deNO_x$ efficiency in the medium temperature range with obviously broadened operation temperature window and enhanced N_2 selectivity. For example, the deposition of only 1% WO_x onto Fe_2O_3 could promote the NH_3-SCR activity to a certain extent above 250 °C. It should be noted that, on Fe_2O_3 and 1% WO_x/Fe_2O_3 samples, the NO_x conversion at *ca.* 350 and 400 °C showed negative values, and this was probably caused by the over-oxidation of NH_3 (to
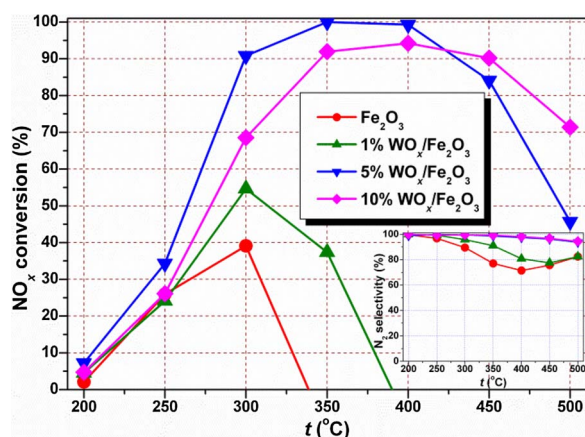
Fig. 1. The NO$_x$ conversion as a function of reaction temperature in NH$_3$-SCR reaction over δ% WO$_x$/Fe$_2$O$_3$ serial catalysts (δ = 0, 1, 5, 10) under the GHSV of 50,000 h^{-1}.

NO or NO$_2$) at high temperatures. Significantly, with over 80% NO$_x$ conversion can be obtained from 300 to 450 °C over the optimal 5% WO$_x$/Fe$_2$O$_3$ catalyst along with greatly improved N$_2$ selectivity. Further increasing the WO$_x$ deposition amount to 10% led to some decrease of deNO$_x$ activity below 400 °C possibly due to the aggregation of WO$_x$ species or the excessive coverage of catalytically active sites, which will be verified in the following characterization sections.

For practical use on diesel engines, high SO$_2$ durability is usually required for the potential NH$_3$-SCR catalysts. Choosing the 5% WO$_x$/Fe$_2$O$_3$ catalyst as the optimal candidate, we have systematically investigated its SO$_2$ durability not only at a fixed temperature point but also in the whole temperature range. As shown in Fig. 2A, the introduction of 100 ppm SO$_2$ into the SCR atmosphere did not influence the deNO$_x$ efficiency over the 5% WO$_x$/Fe$_2$O$_3$ catalyst at 300 °C, and the NO$_x$ conversion could always maintain above 80% even after 24 h reaction. The NH$_3$-SCR activity of the sulfated 5% WO$_x$/Fe$_2$O$_3$ catalyst as a function of reaction temperature was also tested in comparison with the fresh one, and the results are shown in Fig. 2B. No obvious difference in the SCR activity can be observed over the fresh and sulfated 5% WO$_x$/Fe$_2$O$_3$ catalyst, indicating that this WO$_x$ promoted Fe$_2$O$_3$ catalyst is highly resistant to the SO$_2$ poisoning which is very beneficial to its practical use.

The influences of H$_2$O and space velocity on the NO$_x$ conversion over 5% WO$_x$/Fe$_2$O$_3$ were also tested (Fig. 3). Different effects of the presence of 5% H$_2$O in the feeding gas on the NO$_x$ conversion were observed at low temperature and high temperature, respectively. The
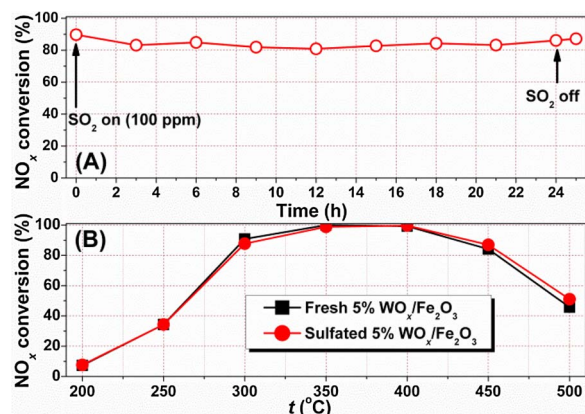

Fig. 2. (A) The NO$_x$ conversion as a function of reaction time in NH$_3$-SCR reaction over 5% WO$_x$/Fe$_2$O$_3$ catalyst in the presence of 100 ppm SO$_2$ at 300 °C under the GHSV of 50,000 h^{-1}; (B) The NO$_x$ conversion as a function of reaction temperature in NH$_3$-SCR reaction over fresh and sulphated 5% WO$_x$/Fe$_2$O$_3$ catalysts under the GHSV of 50,000 h^{-1}.
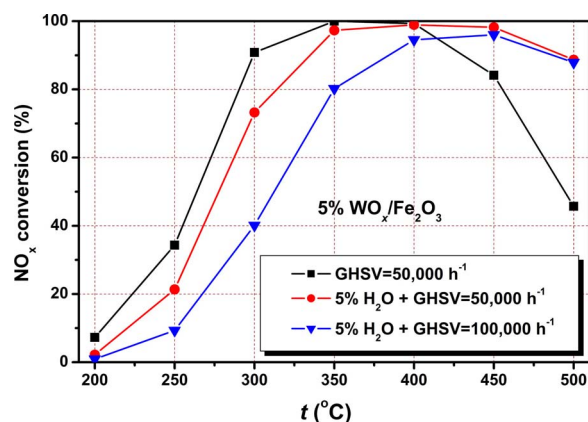

Fig. 3. The influences of H$_2$O and GHSV on the NO$_x$ conversion over 5% WO$_x$/Fe$_2$O$_3$ catalyst.

NO$_x$ conversion was inhibited at low temperature due to the adsorption competition between H$_2$O and reactants (NO$_x$ and NH$_3$) on the surface active sites of the catalyst, while the NO$_x$ conversion was enhanced at high temperature owing to the suppression of the unselective oxidation of NH$_3$. The increase of GHSV from 50,000 h^{-1} to 100,000 h^{-1} induced a further decrease of NO$_x$ conversion at low temperature, but the NO$_x$ conversion of over 80% could still be obtained in the typical temperature range of diesel exhaust (from 350 to 500 °C).

3.2. Surface areas and pore parameters

Derived from the N$_2$ physisorption results, the textural parameters of δ% WO$_x$/Fe$_2$O$_3$ serial catalysts including BET surface areas, pore volumes and pore radii are shown in Table 1. With the increase of WO$_x$ deposition amount, both the BET surface areas and pore volumes of δ% WO$_x$/Fe$_2$O$_3$ catalysts (δ = 1, 5, 10) only showed some slight decrease to a certain extent, mainly due to the blocking of partial pore channels of Fe$_2$O$_3$ by the deposited WO$_x$ species. If normalized by the BET surface areas, the promotion effect of WO$_x$ deposition on the NH$_3$-SCR activity of Fe$_2$O$_3$ will be more obvious. It is interesting that the optimal 5% WO$_x$/Fe$_2$O$_3$ catalyst exhibited the largest pore radius, which was possibly due to the presence of abundant WO$_x$ species on this sample with relatively high dispersion degree thus obtaining more extra piled pores with larger radius.

3.3. Bulk structure of Fe$_2$O$_3$ characterized by XRD and XAFS

To investigate the influence of WO$_x$ deposition on the crystal structure of Fe$_2$O$_3$, both the XRD patterns and Fe-K XAFS including XANES and EXAFS were measured, as the results shown in Figs. 4, S1 and S2, respectively. Before and after WO$_x$ deposition, no obvious difference in the diffraction peaks of hematite α-Fe$_2$O$_3$ can be observed (Fig. 4), indicating that the surface modification of Fe$_2$O$_3$ did not influence its bulk structure at all. At the same time, no diffraction peaks

Table 1
Textural parameters of δ% WO$_x$/Fe$_2$O$_3$ serial catalysts (δ = 1, 5, 10) and Fe$_2$O$_3$, WO$_3$ reference samples.

Samples	S$_{BET}$ [m^2 g^{-1}][a]	Pore volume [cm^3 g^{-1}][b]	Pore radius [nm][c]
Fe$_2$O$_3$	24.1	0.31	1.5
1% WO$_x$/Fe$_2$O$_3$	24.9	0.32	2.4
5% WO$_x$/Fe$_2$O$_3$	24.6	0.28	2.8
10% WO$_x$/Fe$_2$O$_3$	23.4	0.26	1.7
WO$_3$	0.01	0.01	1.5

[a] BET surface area.
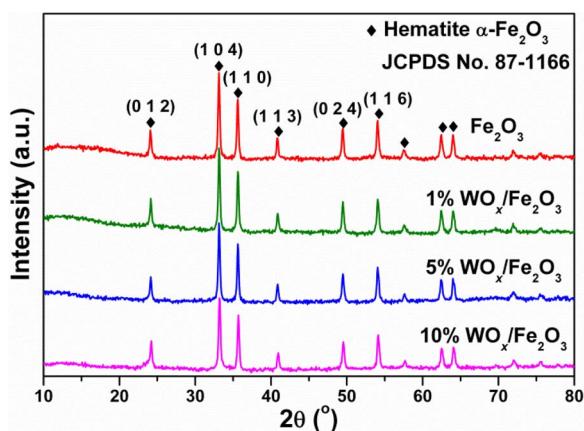[b] BJH desorption pore volume.
[c] BJH adsorption pore radius.

Fig. 4. The powder XRD patterns of $\delta\%$ WO_x/Fe_2O_3 serial catalysts ($\delta = 0, 1, 5, 10$).

attributed to WO_3 can be observed even at high WO_x loading as 10%, suggesting that the possible strong interaction between WO_x and Fe_2O_3 could lead to the relatively high dispersion of WO_x on the Fe_2O_3 surface. Besides, the Fe-K XANES patterns of the WO_x promoted Fe_2O_3 catalysts were identical to that of pristine Fe_2O_3 (Fig. S1A), showing the same absorption edge energy of Fe^{3+} at 7127.1 eV (Fig. S1B). The Fe-K EXAFS of $\delta\%$ WO_x/Fe_2O_3 catalysts ($\delta = 0, 1, 5, 10$) in R space (Fig. S2A) and k space (Fig. S2B) were also quite similar to each other, exhibiting the same Fe−O and Fe−O−Fe coordination shells with similar coordination numbers and bond distances. All the above-mentioned XAFS results indicate again that the surface deposited WO_x species did not enter the lattice of hematite Fe_2O_3 to change its bulk crystal structure, only existing as a surface modifier to possibly influence the microstructure and electronic property in the outermost layers of the catalysts.

3.4. Local structure of WO_x species characterized by XAFS

By measuring the W-L_{III} XANES and EXAFS, the local structure of WO_x species on the Fe_2O_3 surface can be well analyzed, as the results shown in Figs. 5 and 6. In W-L_{III} XANES for all samples (Fig. 5A), the electron transitions from $2p_{3/2}$ orbitals to 5d orbitals are typically presented by the white line, and two overlapped peaks in the white line are observed owing to the splitting of the 5d states by the ligand field [30]. It is interesting to see that, with the increase of WO_x loading, the ratio of the sub-peak in the white line at lower energy position decreased to a certain extent, and in the 10% WO_x/Fe_2O_3 with relatively high WO_x loading, its XANES pattern became closer to that of pristine WO_3. This means that during the increase of WO_x loading amount on Fe_2O_3 surface, the coordination configuration of partial WO_x species might also change probably from tetrahedral structure to octahedral structure, which will be discussed later.

From the first-order derivatives of W-L_{III} XANES in Fig. 5B, it is clear to see that the absorption edge energy of W species in $\delta\%$ WO_x/Fe_2O_3 serial catalysts (10204.5 eV) was 0.5 eV lower than that in pristine WO_3 (10,205.0 eV), indicating that the average valence of the W species in the promoted WO_x/Fe_2O_3 catalysts is actually lower than 6+. This is possibly due to the deviation of electron cloud from surface Fe^{3+} to W^{6+} through an electronic inductive effect as we described in our previous studies [31–33], resulting in the formation of $W^{(6-\delta)+}$ and $Fe^{(3+\delta)+}$ species on the catalyst surface. The XPS results in the following section will help to check if such electronic inductive effect is indeed present between surface Fe and W species.

Back to the W-L_{III} XANES, Fig. 5C shows the second-order derivatives of XANES patterns for all samples to better discriminate the two split peak positions in the white line. The gap energy between the sub-peaks at higher and lower energy positions can also be determined, with this value being *ca.* 3.96 eV for $\delta\%$ WO_x/Fe_2O_3 serial catalysts and

4.52 eV for pristine WO_3. Yamazoe et al. [30] concluded in their work that this gap energy would increase as the local coordination structure of WO_x species changing from tetrahedron (-WO_4) to octahedron (-WO_6). Therefore, we can conclude that with the increase of WO_x loading amount, the ratio of -WO_4 species in the WO_x/Fe_2O_3 catalysts actually decreased and at the same time the ratio of -WO_6 species increased. The optimal 5% WO_x/Fe_2O_3 catalyst should have a well balanced ratio of -WO_4/-WO_6 species thus showing the most excellent NH_3-SCR performance.

Fig. 6A shows the EXAFS results of W-L_{III} edge in R space for $\delta\%$ WO_x/Fe_2O_3 serial catalysts and pristine WO_3 together with the simulated EXAFS results of WO_3 and Fe_2WO_6 using FEFF8.4 code. All the W species in $\delta\%$ WO_x/Fe_2O_3 serial catalysts and pristine WO_3 exhibited the first W−O coordination shells with similar bond distances, yet quite different coordination shells above 2.0 Å were observed. For 1% WO_x/Fe_2O_3 catalyst, only a well defined coordination peak attributed to the W−O plus W−O−Fe scattering pathways can be found, indicating that at low WO_x loading the WO_x species could well disperse on the Fe_2O_3 surface without the formation of aggregated WO_x clusters at all. With the increase of WO_x loading amount to 5 and 10%, the coordination shells ascribed to W−O−W can be well identified at *ca.* 3.5 Å similar to that in WO_3 besides of the shells owing to W−O plus W−O−Fe scatterings and W−O multiple scatterings. The WO_x species must be present on the Fe_2O_3 surface in oligomeric form under such circumstances, which can be verified by the EXAFS curve fitting results as shown in Fig. 6B. By using the W−O−W scattering pathway from WO_3 model, the coordination shells in 5% WO_x/Fe_2O_3, 10% WO_x/Fe_2O_3 and pristine WO_3 in the dashed rectangle in Fig. 6A can be simulated with high fitting degree, obtaining the coordination numbers of 2.4, 2.8 and 4.0, respectively, with the bond lengths at 3.83–3.86 Å. These results clearly suggest that with the increase of WO_x loading amount, the particle size of the oligomeric WO_x on Fe_2O_3 surface gradually increased, and on the optimal 5% WO_x/Fe_2O_3 catalyst the WO_x species was mainly present in the form of dimeric or trimeric clusters. Such an unsaturated coordination state of W−O−W on the catalyst surface represents the existence of abundant local W defects which can be hydroxylated by H_2O to form W−O−H species, acting as the Brønsted acid sites for NH_3 adsorption in SCR reaction.

3.5. Surface composition and electronic inductive effect characterized by XPS

The surface compositions of $\delta\%$ WO_x/Fe_2O_3 serial catalysts were characterized by XPS, as the results shown in Fig. 7 and Table 2. With the increase of WO_x loading amount from 1% to 10%, the XPS peak intensities of W 4f (Fig. 7A) showed a monotonic increase to a certain extent, and at the same time the XPS peak intensities of Fe 2p (Fig. 7B) showed a gradual decrease, which was mainly due to the coverage of Fe_2O_3 surface by the deposited WO_x species. As the semi-quantitative analysis results of the surface atomic concentrations shown in Table 1, the surface W concentration increased from 2.9% on 5% WO_x/Fe_2O_3 catalyst to 4.1% on 10% WO_x/Fe_2O_3 catalyst, while the surface Fe concentrations on these two catalysts were nearly the same (37.5% *vs.* 37.1%). These results indicate that the 5% WO_x loading amount might have already reached the threshold value for the total coverage of Fe_2O_3 surface by WO_x species, and further increasing the WO_x loading amount only led to the formation of multiple WO_x layers or surface converged clusters thus resulting in the decrease of NH_3-SCR performance. Besides, the deconvoluted XPS peaks of O 1s are shown in Fig. 7C, and the relative concentrations of different oxygen species (O_β at 529.5–530.7 eV, O_α at 530.8–531.6 eV, surface OH groups at 533.1–532.9 eV probably resulting from chemisorbed H_2O) [34] are presented in Table 1. It is noteworthy that with the increase of WO_x loading amount, the binding energy of O_β on $\delta\%$ WO_x/Fe_2O_3 catalysts showed some increase comparing to pure Fe_2O_3, and we consider that this was mainly caused by the intrinsic higher binding energy of O_β on
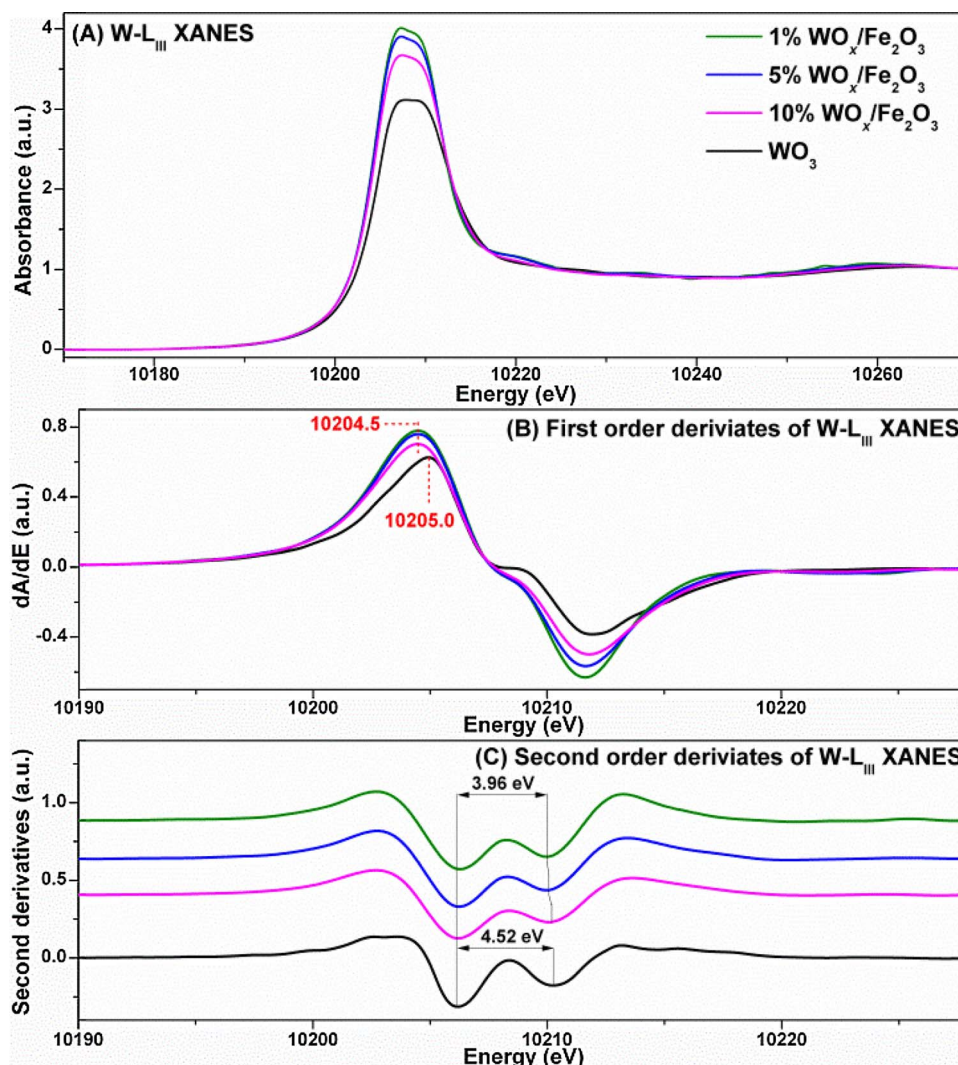
Fig. 5. (A) Normalized XANES spectra of W L_{III}-edge in W-containing samples, (B) corresponding first-order derivatives and (C) corresponding second-order derivatives.

WO_x species than that on Fe_2O_3 (530.7 *vs.* 529.5 eV). Importantly, as we can clearly see, the deposition of WO_x onto Fe_2O_3 surface could greatly facilitate the formation of surface hydroxyls, and the optimal 5% WO_x/ Fe_2O_3 catalyst exhibited the most abundant surface OH groups acting as efficient Brønsted acid sites for NH_3 adsorption to supply sufficient reductant on the catalyst surface for NO_x reduction in SCR reaction.

The W-L_{III} XANES results in Fig. 5B have already shown that the average valence state of W species in δ% WO_x/Fe_2O_3 serial catalysts was relatively lower than that in pristine WO_3, and this phenomenon was much more obvious in W 4f XPS results. As clearly shown in Fig. 7A, both the binding energies of W $4f_{7/2}$ (35.1–35.5 eV) and W $4f_{5/2}$ (37.2–37.7 eV) on δ% WO_x/Fe_2O_3 catalysts were indeed lower than the corresponding values on pristine WO_3 sample (W $4f_{7/2}$ at 35.8 eV and W $4f_{5/2}$ at 38.0 eV) [35,36], and with the increase of the WO_x loading amount on the promoted catalysts, the binding energies of W 4f gradually increased approaching the values on pristine WO_3. Feng et al. [37] also observed that the as-prepared monolayer-dispersed WO_x species on α-Fe_2O_3 (0001) surface had mixed oxidation states of W^{6+} and W^{5+}. At the same time, as shown in Fig. 7B, the deposition of WO_x species onto Fe_2O_3 surface also resulted in the increase of binding energies of both Fe $2p_{3/2}$ (710.9–711.0 eV) and Fe $2p_{1/2}$ (724.3–724.4 eV) on δ% WO_x/Fe_2O_3 catalysts comparing with that on pristine Fe_2O_3 (Fe $2p_{3/2}$ at 710.8 eV and Fe $2p_{1/2}$ at 724.1 eV) [38,39]. Interestingly, this effect already reached the limit when the WO_x loading amount was above 5%, which was mainly due to the occurrence of surface

convergence of WO_x species without further contacting the surface Fe species. The above-mentioned XPS results well elucidated that the electronic inductive effect between surface W^{6+} and Fe^{3+} species was certainly present on WO_x/Fe_2O_3 catalysts through the formation of W–O–Fe bonds, resulting in the generation of $W^{(6-δ)+}$ and $Fe^{(3+δ)+}$ species simultaneously. During this process, the oxidation ability of the surface Fe species was actually enhanced to a certain extent, which was beneficial to the activation of reactants for NH_3-SCR reaction (mainly for NH_3 activation).

3.6. The variation of redox ability induced by WO_x deposition

The NH_3-SCR reaction usually requires a redox cycle of active sites in SCR catalysts to activate the reactants efficiently. Too low redox ability will result in the low deNO$_x$ efficiency, while too high redox ability may lead to unselective oxidation of NH_3 thus resulting in the lack of reducing agents and poor N_2 selectivity. Therefore, an appropriate redox ability of NH_3-SCR catalysts such as the WO_x/Fe_2O_3 catalyst in this study is highly desired, which can be characterized by the H_2-TPR experiments in combination with the *in situ* Fe-K XAFS to determine the phase transformation of Fe species simultaneously.

As shown in Fig. 8, the H_2-TPR profile of pristine Fe_2O_3 contained two composite peaks, thus the peak deconvolution followed by calculation of H_2 consumption ratios was conducted to better confirm its reduction process (Table 3). According to the calculated area ratios of
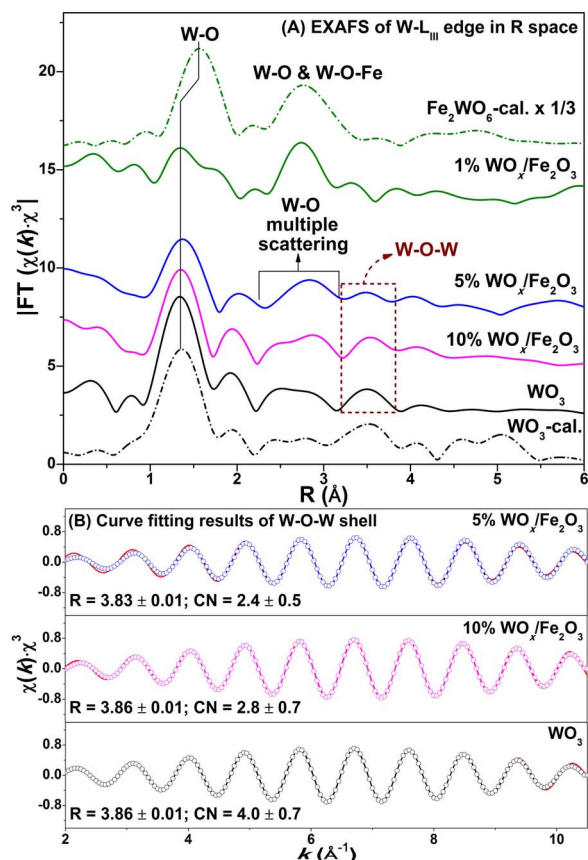
Fig. 6. EXAFS spectra of W L$_{III}$-edge in W-containing samples: (A) Fourier transforms of filtered $k^3\chi(k)$ into R space, where the dashed lines correspond to the calculated EXAFS results of WO$_3$ and Fe$_2$WO$_6$ in R space using FEFF8.4 code; (B) W L$_{III}$-edge EXAFS oscillations in 5% WO$_x$/Fe$_2$O$_3$, 10% WO$_x$/Fe$_2$O$_3$ and WO$_3$ samples in the R range of *ca.* 3.1–3.9 Å, where the dotted lines correspond to the calculated EXAFS oscillations of W−O−W bond in WO$_3$ using FEFF8.4 code.
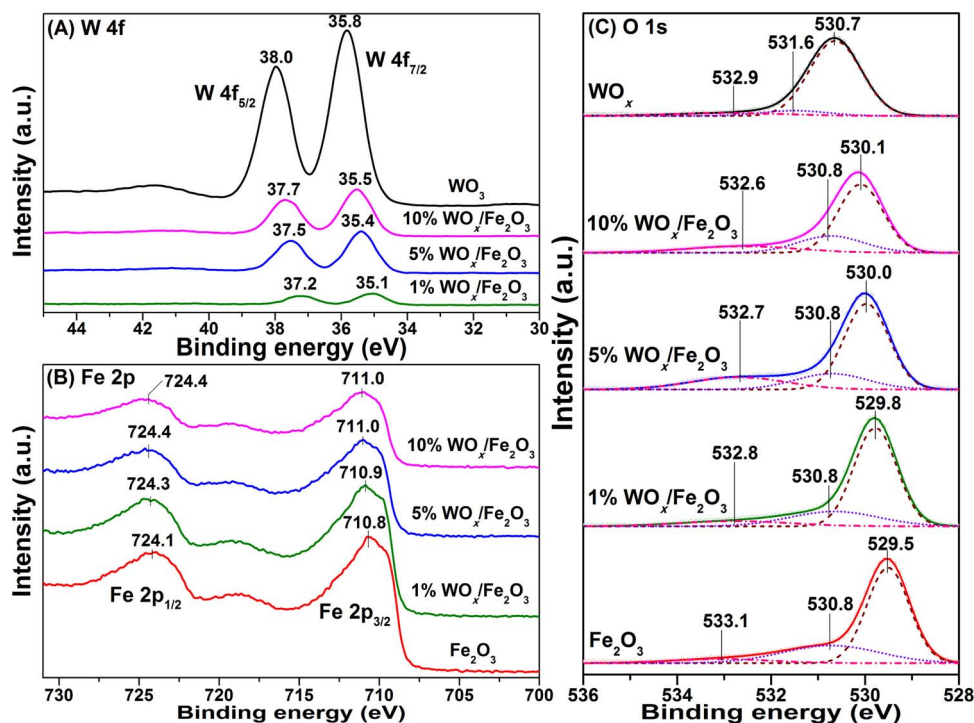
Table 2

Semi-quantitative analysis of surface atomic concentrations (% in molar ratio) over δ% WO$_x$/Fe$_2$O$_3$ serial catalysts (δ = 1, 5, 10) and Fe$_2$O$_3$, WO$_3$ reference samples derived from XPS data.

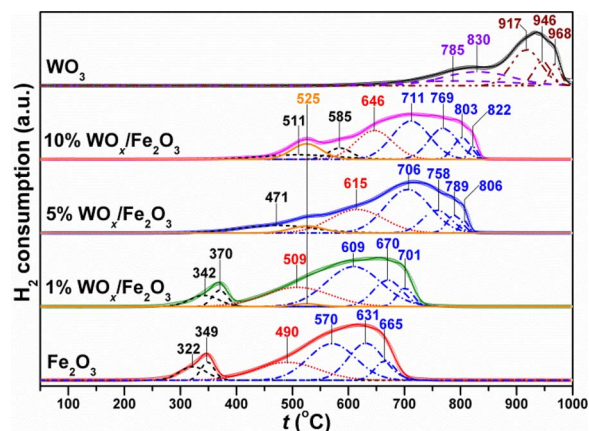| Samples	W (%)	Fe (%)	O (%)	OH/(O$_\beta$ + O$_\alpha$ + OH) (%)
Fe$_2$O$_3$	–	49.0	51.0	6.5
1% WO$_x$/Fe$_2$O$_3$	0.7	47.5	51.8	9.5
5% WO$_x$/Fe$_2$O$_3$	2.9	37.5	59.7	19.1
10% WO$_x$/Fe$_2$O$_3$	4.1	37.1	58.8	14.6
WO$_3$	23.3	–	76.7	7.1

Fig. 8. H$_2$-TPR results of δ% WO$_x$/Fe$_2$O$_3$ serial catalysts (δ = 1, 5, 10) and Fe$_2$O$_3$, WO$_3$ reference samples.

the sub-bands at relatively low (I), medium (II) and high (III) temperatures, which was 11.8:21.9:66.3 for pristine Fe$_2$O$_3$, the Fe species in this sample probably mainly followed a three-step reduction process: Fe$_2$O$_3$ → Fe$_3$O$_4$ → FeO → Fe [40–42]. It is interesting to observe that the deposition of only 1% WO$_x$ onto the Fe$_2$O$_3$ surface could already delay the reduction process of Fe$_2$O$_3$ towards high temperature range, and as we can clearly see this delay effect was much more obvious on 5% and

Fig. 7. XPS results of (A) W 4f, (B) Fe 2p, and (C) O 1s in δ% WO$_x$/Fe$_2$O$_3$ serial catalysts (δ = 1, 5, 10) together with Fe$_2$O$_3$, WO$_3$ reference samples.

Table 3
The calculated area ratios of sub-bands derived from the deconvoluted H$_2$-TPR profiles of δ% WO$_x$/Fe$_2$O$_3$ serial catalysts (δ = 1, 5, 10) and Fe$_2$O$_3$, WO$_3$ reference samples.

Samples	Area ratio I (%)	Area ratio II (%)	Area ratio III (%)	Area ratio IV (%)	Area ratio V (%)	Area ratio VI (%)
Fe$_2$O$_3$	I$_{(322 + 349)}$	II$_{490}$	III$_{(570 + 631 + 665)}$	–	–	–
	11.8	21.9	66.3	–	–	–
1% WO$_x$/Fe$_2$O$_3$	I$_{(342 + 370)}$	II$_{509}$	III$_{(609 + 670 + 701)}$	IV$_{525}$	–	–
	11.1	24.6	62.8	1.4	–	–
5% WO$_x$/Fe$_2$O$_3$	I$_{471}$	II$_{615}$	III$_{(706 + 758 + 789 + 806)}$	IV$_{525}$	–	–
	11.2	24.9	59.4	4.5	–	–
10% WO$_x$/Fe$_2$O$_3$	I$_{(511 + 585)}$	II$_{646}$	III$_{(711 + 769 + 803 + 822)}$	IV$_{525}$	–	–
	12.2	21.6	56.8	9.5	–	–
WO$_3$	–	–	–	–	V$_{(785 + 830)}$	VI$_{(917 + 946 + 968)}$
	–	–	–	–	46.9	53.1

10% WO$_x$/Fe$_2$O$_3$ catalysts. Based on the calculated H$_2$ consumption area ratios of I:II:III which were *ca.* 1:2:6 for δ% WO$_x$/Fe$_2$O$_3$ serial catalysts, it can be concluded that the three-step reduction mechanism was not influenced by the WO$_x$ deposition at all, but the reducibility of Fe species in the bulk phase was actually tuned towards high temperature range. We have already mentioned that the formation of W$^{(6-\delta)+}$−O−Fe$^{(3+\delta)+}$ on the catalyst surface could result in the enhancement of oxidation ability of the surface Fe species (the reduction of this small portion of surface Fe species cannot be distinguished from H$_2$-TPR profiles comparing to the larger portion of bulk Fe$_2$O$_3$), and we can consider these types of surface Fe species as well dispersed monomeric Fe similar as that in Fe-zeolite materials with high deNO$_x$ efficiency [43,44]. While the catalytic performance of the bulk Fe$_2$O$_3$ in NH$_3$-SCR reaction and NH$_3$ oxidation was quite similar to the severely clustered Fe$_x$O$_y$ species in Fe-zeolite materials with high Fe loading or low Fe dispersion degree, which can cause the unselective consumption of reducing agent NH$_3$ in SCR reaction thus leading to the low deNO$_x$ activity and poor N$_2$ selectivity [43,45,46]. In this study, the simple deposition of WO$_x$ species onto Fe$_2$O$_3$ surface could effectively inhibit the over-oxidation ability of bulk Fe$_2$O$_3$, which is a quite interesting and important phenomenon for its practical use in NH$_3$-SCR process. It should be noted that at *ca.* 525 °C, the deconvoluted peaks with the IV area ratios being 1.4%, 4.5% and 9.5% for 1%, 5% and 10% WO$_x$/Fe$_2$O$_3$ catalysts, respectively, can be also found, which should be due to the reduction of WO$_x$ species on the Fe$_2$O$_3$ surface [47,48]. The effective dispersion along with the strong interaction between surface WO$_x$ species and Fe$_2$O$_3$ greatly lowered the reduction temperature of WO$_x$ species possibly owing to the formation of W−O−Fe bonds comparing with that of pristine WO$_3$ (probably following a WO$_3$ → W$_2$O$_5$ → WO$_2$ reduction process judging from the area ratios of V:VI), indicating again that the deposition of WO$_x$ onto Fe$_2$O$_3$ not only changed the reducibility of Fe$_2$O$_3$ but also varied its own reducibility.

To better confirm the phase transformation process of Fe$_2$O$_3$ in δ% WO$_x$/Fe$_2$O$_3$ serial catalysts during the H$_2$-TPR experiments, the *in situ* Fe-K XAFS including XANES and EXAFS were recorded. Comparing with the XAFS results of Fe-containing reference samples (Fig. S3) and judging from the *in situ* XANES (Fig. S4) and *in situ* EXAFS (Fig. 9) of Fe-K edge in WO$_x$/Fe$_2$O$_3$ catalysts, the reduction process of Fe$_2$O$_3$ can be clearly determined, which indeed followed the three-step procedures as we mentioned above. For pristine Fe$_2$O$_3$ sample, the Fe species could be totally converted into Fe$_3$O$_4$ at as low as 400 °C, into FeO at 550 °C and finally into metallic Fe at 900 °C. However, for 1% WO$_x$/Fe$_2$O$_3$ catalyst, the Fe$_2$O$_3$ could be reduced to Fe$_3$O$_4$ at 450 °C and then into FeO at 600 °C, which were *ca.* 50 °C higher than the corresponding reduction temperatures of pristine Fe$_2$O$_3$. For 5% and 10% WO$_x$/Fe$_2$O$_3$ catalysts, it seemed that the delay effect on the reducibility of Fe species induced by WO$_x$ deposition have already reached the maximum, and the corresponding reduction temperatures resulting in the transformation of Fe$_2$O$_3$ into Fe$_3$O$_4$ and then into FeO were delayed to 550 and 700 °C (*i.e.* *ca.* 150 °C higher), respectively. These results clearly suggest that the simple deposition of WO$_x$ species onto Fe$_2$O$_3$ surface could effectively

adjust the redox ability of Fe$_2$O$_3$ especially in the bulk phase, which is in well accordance with the conclusions drawn from the H$_2$-TPR profiles. In the activity test over 5% WO$_x$/Fe$_2$O$_3$ catalyst, the NO$_x$ conversion can maintain above 80% from 300 to 450 °C, and in this temperature range the active Fe sites should have an appropriate redox cycle between Fe^{3+} ↔ Fe^{2+} species during the NH$_3$-SCR reaction. The proper deposition of WO$_x$ onto Fe$_2$O$_3$ effectively created such a circumstance through the formation of W−O−Fe species together with the tuning of the reducibility of bulk Fe$_2$O$_3$, which is an important reason for the significant promotion of NH$_3$-SCR performance.

3.7. The variation of NH$_3$/NO adsorption ability and oxidation activity induced by WO$_x$ deposition

The NH$_3$/NO adsorption and oxidation behaviors are important processes in the NH$_3$-SCR reaction. Therefore, the influence of WO$_x$ deposition onto Fe$_2$O$_3$ surface on these processes was investigated in detail using *in situ* DRIFTS and activity test methods, and the results are shown in Figs. 10 and 11, respectively.

As shown in Fig. 10A, after NH$_3$ adsorption and N$_2$ purge, the infrared bands characteristics of NH$_3$ adsorbed species over pristine Fe$_2$O$_3$ were observed, including the NH$_4^+$ species on Brønsted acid sites at 1684 and 1439 cm^{-1} due to the δ_s and δ_{as} vibration modes, respectively [49–53], and the coordinated NH$_3$ species on Lewis acid sites at 1606 and 1192 cm^{-1} due to the δ_{as} and δ_s vibration modes, respectively [17,49,54,55]. Besides, some overlapped IR bands in the range of 1350–1380 cm^{-1} can also be observed, and the assignment of these species was quite complicated and diverse as described in previous studies. For example, some researchers assigned these bands to coordinated NH$_3$ with asymmetric bending vibration mode [56], and others ascribed them to amide (−NH$_2$) species with wagging vibration mode in hydrazine (which resulted from the dehydrogenation of NH$_3$ following by dimerization) [49,57,58] or to the highly oxidized species such as nitrates or nitrites [54]. However, in this study, based on the reactivity examination of these surface species in the subsequent Section 3.8 during the various transient reaction conditions also using the *in situ* DRIFTS method, these overlapped bands can actually be assigned to the ionic NH$_4^+$ species with different bending vibration modes from that of the common NH$_4^+$ species as detected at 1684 and 1439 cm^{-1} [59–63]. It has been reported that the feature of these species was generated by the difference in NH$_4^+$ symmetry resulting from the different hydrogen bonds with the neighboring oxygen atoms or NH$_3$ molecules [62,64,65]. Overall, it should be noted that the amount of NH$_3$ adsorbed species on Lewis acid sites was much higher than that on Brønsted acid sites, and the N−H stretching vibration bands at 3122, 3223, 3336 and 3390 cm^{-1} also confirmed the dominant presence of coordinated NH$_3$ on Fe$_2$O$_3$ surface [49,66]. These results are in good accordance with the conclusions drawn by Ramis et al. [54,67] that the Fe$_2$O$_3$ material does not carry enough Brønsted acidity. The coordinated NH$_3$ on Lewis acid sites of Fe$_2$O$_3$ could undergo the hydrogen abstraction process to form −NH$_2$ species with the scissoring vibration
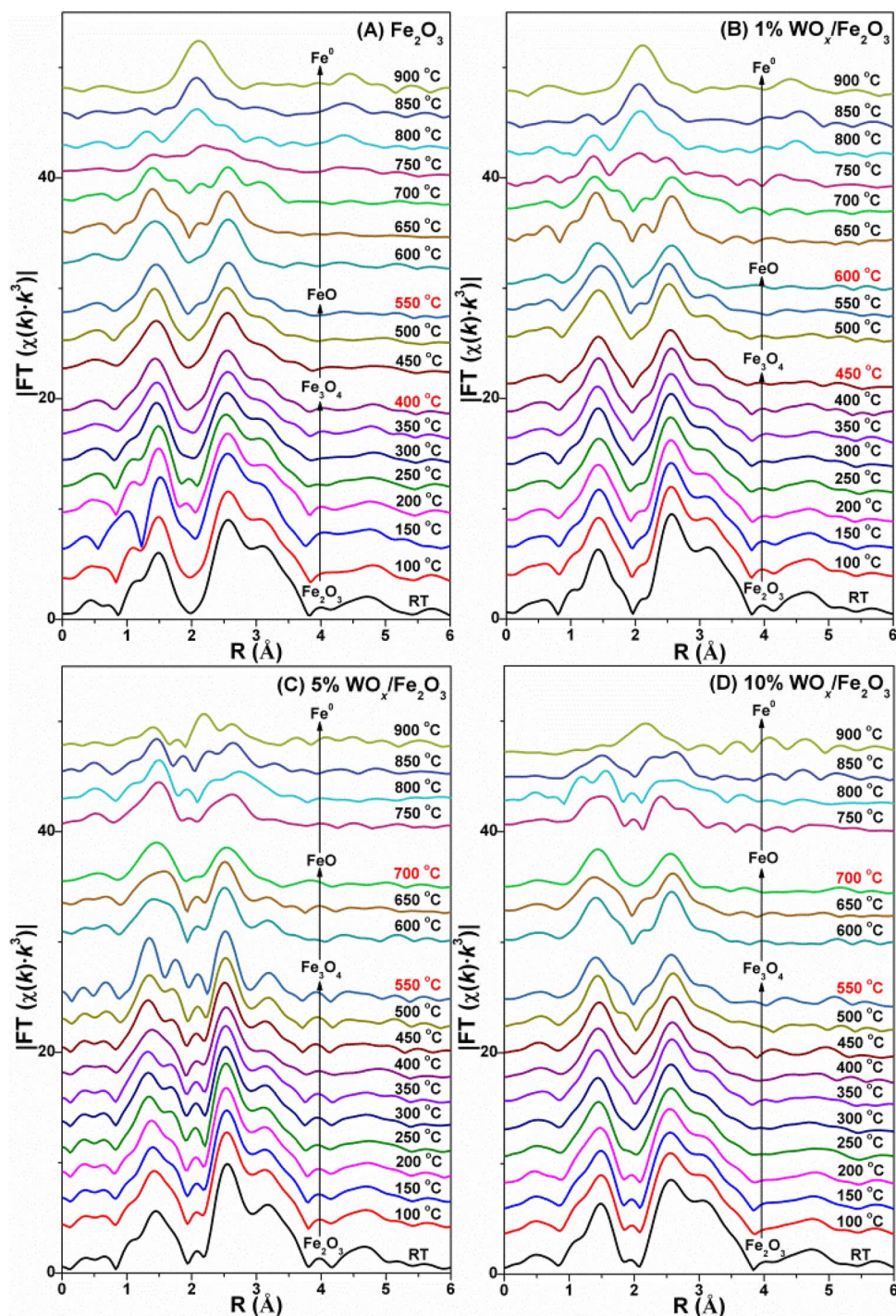
Fig. 9. *In situ* EXAFS spectra of Fe K-edge in (A) Fe$_2$O$_3$, (B) 1% WO$_x$/Fe$_2$O$_3$, (C) 5% WO$_x$/Fe$_2$O$_3$ and (D) 10% WO$_x$/Fe$_2$O$_3$ during the reduction process by H$_2$.

mode detected at 1516 cm^{-1} [49,68,69], and the formed $-$NH$_2$ species could react with gaseous NO to form NH$_2$NO and then decompose to N$_2$ and H$_2$O contributing to the total SCR reaction. This is possibly the reason for the SCR activity achieved on pristine Fe$_2$O$_3$, although the operation temperature window was rather narrow. Over the 1% WO$_x$/Fe$_2$O$_3$ catalyst, after the NH$_3$ adsorption and N$_2$ purge, the NH$_4^+$ species showed some decrease to a certain extent possibly due to the occupation of some Brønsted acid sites by WO$_x$ on Fe$_2$O$_3$; and at the same time, the band ascribed to coordinated NH$_3$ species (1188 cm^{-1}) broadened to a certain extent, indicating that the induced WO$_x$ species could also act as extra Lewis acid sites in the form of W=O for NH$_3$ adsorption. When the WO$_x$ deposition amount onto Fe$_2$O$_3$ surface was

increased to 5%, the adsorption amount of ionic NH$_4^+$ species (3026, 1676, 1425, 1383 cm^{-1}) was greatly promoted suggesting that the oligomeric WO$_x$ species on Fe$_2$O$_3$ surface could supply abundant Brønsted acid sites in the form of W$-$OH for NH$_3$ adsorption; the obvious consumption bands of surface acidic hydroxyls at 3724 and 3647 cm^{-1} with stretching vibration modes [70] and around 1011 cm^{-1} with deformation vibration modes [71] can also clearly prove this point of view. And meanwhile, the adsorption of coordinated NH$_3$ species on Lewis acid sites was also rich owing to the increase of W=O site numbers. It should be noted that the band owing to the $-$NH$_2$ species at 1529 cm^{-1} [49] can also be observed on the 5% WO$_x$/Fe$_2$O$_3$ catalyst, implying that the activation process of coordinated NH$_3$

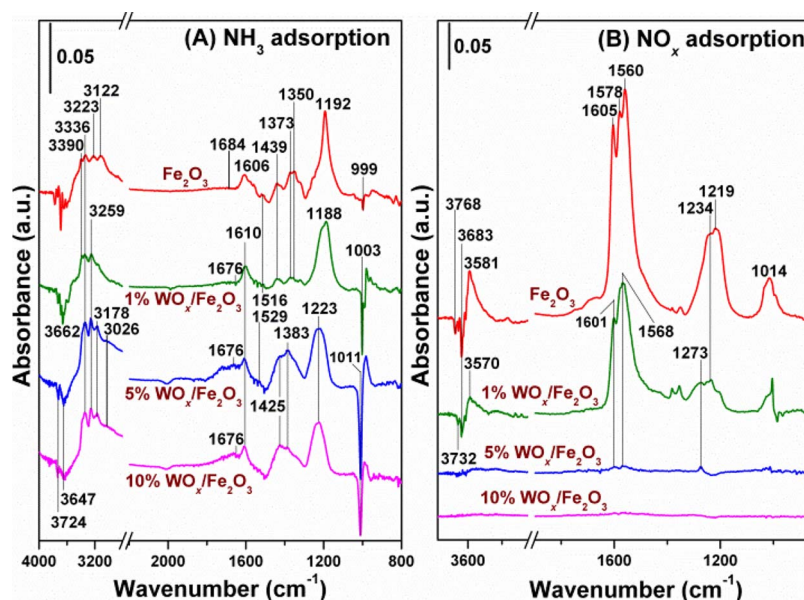**Fig. 10.** *In situ* DRIFTS results (A) NH$_3$ adsorption and (B) NO$_x$ adsorption at 200 °C over δ% WO$_x$/Fe$_2$O$_3$ serial catalysts (δ = 0, 1, 5, 10).

species was not severely inhibited by the deposited WO$_x$ species. In another word, the deposited WO$_x$ species played an important role as efficient NH$_3$ storage reservoir, and the enhanced oxidation ability of Fe species in surface W$^{(6-\delta)+}$−O−Fe$^{(3+\delta)+}$ structure resulted in the easy activation of adsorbed NH$_3$ species, which is beneficial to the total SCR reaction. However, with relatively higher WO$_x$ deposition amount on Fe$_2$O$_3$ surface such as 10%, both the ionic NH$_4^+$ and coordinated NH$_3$ species even showed some slight decrease in intensity, mainly due to the aggregation and structural transformation of WO$_x$ species resulting in the decrease of exposed W−OH and W═O sites. Therefore, the proper deposition amount of WO$_x$ species on Fe$_2$O$_3$ surface (*i.e.* 5%) is very important to keep the abundance and balance of acid sites on the catalyst surface leading to the highest NH$_3$-SCR performance.

Fig. 10B shows the influence of WO$_x$ deposition amount on the NO$_x$ adsorption ability of WO$_x$/Fe$_2$O$_3$ catalysts. As we can clearly see, after NO + O$_2$ adsorption and N$_2$ purge, the infrared bands attributed to monodentate nitrate (1560 and 1234 cm^{-1}), bidentate nitrate (1578 cm^{-1}), bridging nitrate (1605 and 1219 cm^{-1}) [69,72–74] and

cis-(N$_2$O$_2$)$^{2-}$ species (1014 cm^{-1}) [68,75–77] showed up on pristine Fe$_2$O$_3$ surface, together with the consumption bands of surface basic hydroxyls at 3768 and 3683 cm^{-1} [70,78] and the H$_2$O formation band at 3581 cm^{-1} with O−H stretching vibration mode [79]. It is quite obvious that even with only 1% WO$_x$ deposition amount on the Fe$_2$O$_3$ surface, the NO$_x$ adsorption ability was severely inhibited to a certain extent which can be verified by the apparent decrease of IR band intensities. Over the optimal 5% WO$_x$/Fe$_2$O$_3$ catalyst, only a rather small quantity of monodentate nitrate and bridging nitrate can be observed on the surface, and over the 10% WO$_x$/Fe$_2$O$_3$ catalyst the NO$_x$ adsorption was even totally suppressed. These results clearly indicate that the deposited acidic WO$_x$ species can greatly hinder the adsorption of NO$_x$ on the Fe$_2$O$_3$ surface, and gaseous NO or NO$_2$ may directly participate into the NH$_3$-SCR process reacting with NH$_3$ adsorbed species mainly through an Eley-Rideal (E-R) pathway.

Fig. 11A shows the separate NH$_3$ oxidation results over WO$_x$/Fe$_2$O$_3$ serial catalysts, from which we can clearly see that the NH$_3$ oxidation ability of Fe$_2$O$_3$ was obviously inhibited to a certain extent
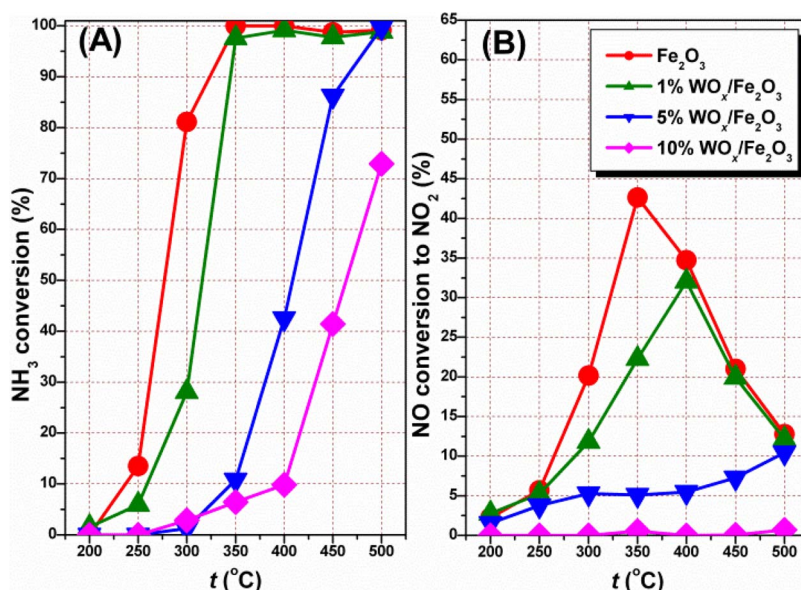

Fig. 11. (A) Separate NH$_3$ oxidation activity and (B) separate NO oxidation activity as a function of reaction temperature over δ% WO$_x$/Fe$_2$O$_3$ serial catalysts (δ = 0, 1, 5, 10).

monotonically as a function of WO_x surface deposition amount, although the NH_3 adsorption capacity (especially as ionic NH_4^+ species) of the WO_x modified samples was actually increased (Fig. 10A). This means that more NH_3 adsorbed species could be reserved on the WO_x/Fe_2O_3 catalyst surface acting as reducing agents for the deNO$_x$ process, and at the same time the over-oxidation or the unselective catalytic oxidation of NH_3 was greatly suppressed, which are quite beneficial to the improvement of NH_3-SCR activity and N_2 selectivity simultaneously. In good accordance with the *in situ* DRIFTS results of NO$_x$ adsorption, as shown in Fig. 11B, the separate NO oxidation ability of the δ% WO_x/Fe_2O_3 serial catalysts was also decreased monotonically with the increasing of WO_x deposition amount. Especially, for the 10% WO_x/Fe_2O_3 catalyst, its NO oxidation ability was totally inhibited, yet it still showed considerable NH_3-SCR activity in the medium temperature range (Fig. 1), which indicates again that over the WO_x modified Fe_2O_3 catalyst the NO can directly participate in the NH_3-SCR reaction in gas phase with no necessity to adsorb onto catalyst surface as nitrites or nitrates. In short summary, not only the NH_3 oxidation ability but also the NO oxidation ability of Fe_2O_3 was greatly lowered by the surface deposited WO_x species due to the significant modification of Fe_2O_3 reducibility as concluded above in Section 3.6. It should be noted that, from XPS study, we concluded that the surface Fe species actually showed increased oxidation ability due to the electronic inductive effect in $W^{(6-\delta)+}$ and $Fe^{(3+\delta)+}$ structure, which is beneficial for NH_3 dehydrogenation/activation to form $-NH_2$ intermediate. In separate NH_3 oxidation reaction, the surface Fe sites on WO_x/Fe_2O_3 was much less than that on Fe_2O_3 due to WO_x coverage, and the over-oxidation of NH_3 by bulk Fe_2O_3 was also decreased through WO_x modification, thus the overall NH_3 oxidation was actually decreased. Similarly, for separate NO oxidation reaction, NO could not adsorb onto WO_x/Fe_2O_3 surface at all (also with much less surface Fe sites), thus the NO oxidation activity of WO_x/Fe_2O_3 catalyst was also decreased. This explains the seemingly controversial but reasonable conclusions drawn from XPS and NH_3/NO oxidation results.

3.8. NH_3-SCR reaction mechanism over WO_x/Fe_2O_3 catalyst

To further elucidate the NH_3-SCR reaction mechanism over the optimal 5% WO_x/Fe_2O_3 catalyst, the *in situ* DRIFTS experiments including the reaction between NO + O_2 and pre-adsorbed NH_3 species, the reaction between NH_3 and pre-adsorbed NO$_x$ species, and also the reaction under NH_3 + NO + O_2 atmosphere were carefully conducted in comparison with those on pristine Fe_2O_3, and the results are shown in Figs. 12 and 13.

As shown in Fig. 12A, after NH_3 adsorption and N_2 purge over pristine Fe_2O_3, both the ionic NH_4^+ species and coordinated NH_3 species appeared on the surface. However, after the introduction of NO + O_2, only the coordinated NH_3 species on Lewis acid sites (1606 and 1192 cm^{-1}) disappeared rapidly due to the reaction with NO$_x$ to form N_2 and H_2O (1597 cm^{-1}, which is ascribed to adsorbed H_2O possibly in monomer form) [26,80,81], and at the same time the Fe_2O_3 surface was gradually and dominantly covered by nitrate species (1605, 1578, 1558, 1244, 1219 cm^{-1}) and *cis*-$(N_2O_2)^{2-}$ species (1014 cm^{-1}). Even after 60 min reaction, the ionic NH_4^+ species on Brønsted acid sites (1450 and 1352 cm^{-1}) was still present on Fe_2O_3 surface, indicating that the surface acidic hydroxyls bonding to Fe_2O_3 could not contribute to the NH_3-SCR reaction at all. As we discussed above, as shown in Fig. 12B, after NO + O_2 adsorption and N_2 purge, the nitrate species (1605, 1578, 1558, 1244, 1219 cm^{-1}), *cis*-$(N_2O_2)^{2-}$ species (1014 cm^{-1}) and adsorbed H_2O (3581 cm^{-1}) showed up on Fe_2O_3 surface, and after the introduction of NH_3 the surface species became more complicated. The introduced NH_3 not only could adsorb onto the Fe_2O_3 surface as ionic NH_4^+ (1676, 1439, 1356 cm^{-1}) and coordinated NH_3 (1192 cm^{-1}) but also could react with pre-adsorbed NO$_x$ to form surface ammonium nitrate (NH_4NO_3) at 1524, 1281 and 1250 cm^{-1} [27] along with the obvious formation of adsorbed H_2O in monomer
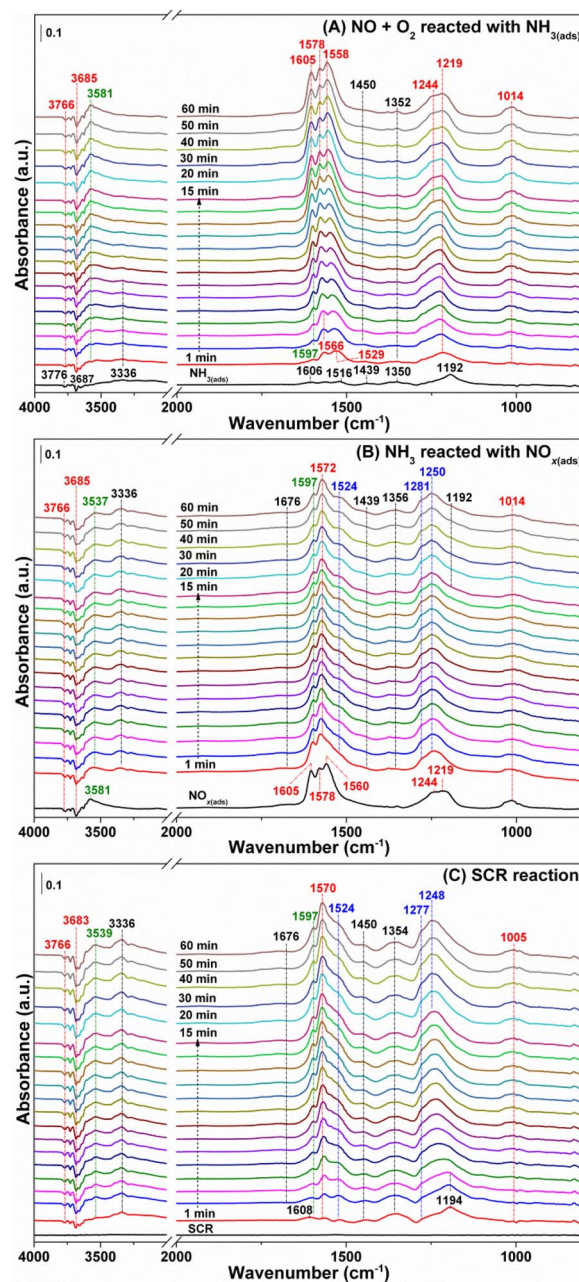

Fig. 12. *In situ* DRIFTS of (A) reaction between NO + O_2 and pre-adsorbed NH_3 species, (B) reaction between NH_3 and pre-adsorbed NO$_x$ species, and (C) reaction in NH_3 + NO + O_2 at 200 °C over pristine Fe_2O_3.

form at 1597 cm^{-1} [26,80,81] and H_2O clusters with hydrogen bonding at 3537 cm^{-1} [26,81,82]. Under the NH_3-SCR reaction condition, as shown in Fig. 12C, the surface NH_4NO_3 species was also obviously detected on Fe_2O_3 surface with a relatively high deposition amount. Over some Mn-containing NH_3-SCR catalysts in our previous study [27,83], the surface NH_4NO_3 species played an important role as reactive intermediate for the deNO$_x$ process especially at low temperatures. However, over this pristine Fe_2O_3 sample, the surface deposited NH_4NO_3 seemed to only act as an inhibitor in the NH_3-SCR reaction possibly because it lacked the catalytic function to promote the reactivity of NH_4NO_3 with NO. It should be noted that only at the beginning of NH_3-SCR reaction (1–3 min) the coordinated NH_3 species could be detected on Fe_2O_3 surface (1194 cm^{-1}), and afterwards the ionic NH_4^+ species (1676, 1450 and 1354 cm^{-1}) and NH_4NO_3 species were steadily present, indicating again that only the Lewis acid sites on
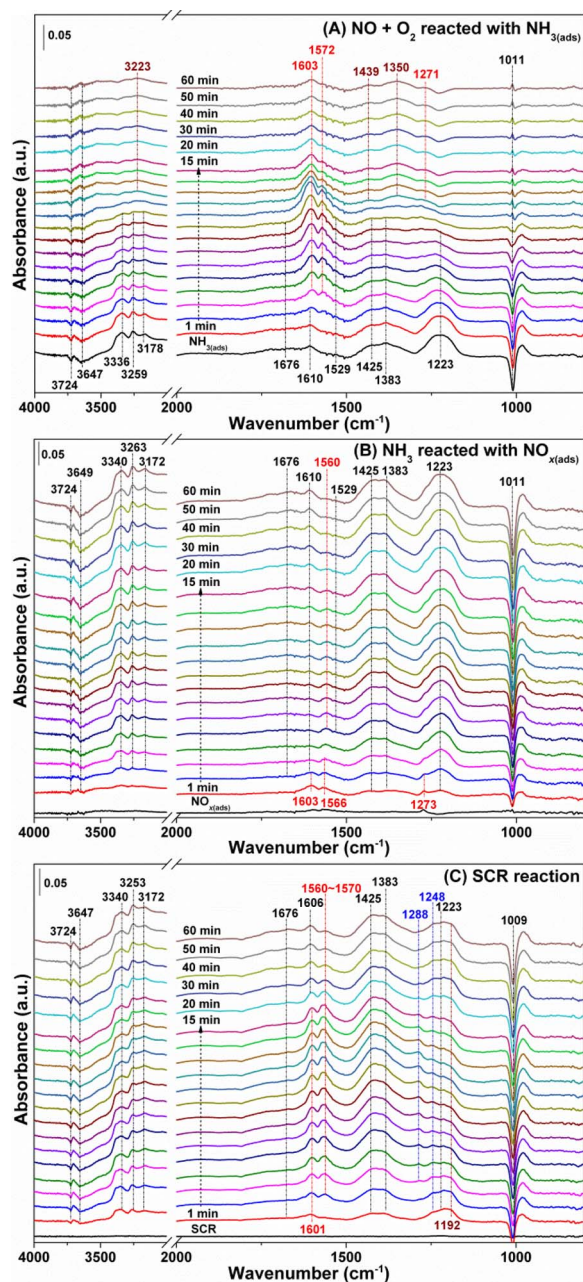
Fig. 13. *In situ* DRIFTS of (A) reaction between NO + O$_2$ and pre-adsorbed NH$_3$ species, (B) reaction between NH$_3$ and pre-adsorbed NO$_x$ species, and (C) reaction in NH$_3$ + NO + O$_2$ at 200 °C over 5% WO$_x$/Fe$_2$O$_3$.

Fe$_2$O$_3$ took part in the NH$_3$-SCR reaction thus showing low deNO$_x$ performance and relatively narrow operation temperature window.

As for the optimal 5% WO$_x$/Fe$_2$O$_3$ catalyst, after NH$_3$ adsorption and N$_2$ purge (Fig. 13A), both ionic NH$_4^+$ species and coordinated NH$_3$ species showed up as usual on surface. Interestingly, after the introduction of NO + O$_2$, not only the coordinated NH$_3$ species (1610, 1223 cm^{-1}) plus the amide species (1529 cm^{-1}), but also the ionic NH$_4^+$ species (1676, 1425, 1383 cm^{-1}) showed obvious decrease in intensity, indicating their participation into the deNO$_x$ process. The gradual recovery of the acidic hydroxyl consumption band at 1011 cm^{-1} could also verify the reactivity of ionic NH$_4^+$ on W−OH sites towards NO. With the increasing of reaction time, a small quantity of nitrate species (1603, 1572 and 1271 cm^{-1}) appeared on the catalyst surface, and surprisingly, some ionic NH$_4^+$ adsorbed on Fe-OH sites (3223, 1439 and 1350 cm^{-1}) could still remain there as spectator. The

above-mentioned results clearly imply that only the coordinated NH$_3$ species on W=O and Fe=O sites and the ionic NH$_4^+$ species on W−OH sites could contribute to the NH$_3$-SCR reaction, while the ionic NH$_4^+$ species on Fe−OH sites was totally inactive in this process. Owing to the severe inhibition of NO$_x$ adsorption by the deposited WO$_x$ species on Fe$_2$O$_3$ surface, as shown in Fig. 13B, only a small amount of bridging nitrates (1603 cm^{-1}) and monodentate nitrates (1566 and 1273 cm^{-1}) could be observed after NO + O$_2$ adsorption and N$_2$ purge. The following introduction of NH$_3$ resulted in the apparent coverage of catalyst surface by ionic NH$_4^+$ and coordinated NH$_3$, and at the same time partial bridging nitrates probably transformed into monodentate nitrates (1560 cm^{-1}) due to the disturbance by adsorbed NH$_3$ species. It is noteworthy that no surface NH$_4$NO$_3$ species was detected in this process at all, which was quite different from that on pristine Fe$_2$O$_3$. Furthermore, under the NH$_3$-SCR reaction atmosphere on 5% WO$_x$/Fe$_2$O$_3$ catalyst, as presented in Fig. 13C, the deposition amount of surface NH$_4$NO$_3$ (1288 and 1248 cm^{-1}) was also much lower than that on pristine Fe$_2$O$_3$, indicating that the inhibition effect of surface NH$_4$NO$_3$ species on the deNO$_x$ performance was actually greatly lowered on the WO$_x$ promoted catalyst. Besides, for the first 15 min reaction, there seemed to be some transformation of bridging nitrates to monodentate nitrates also, and under the steady state reaction condition (60 min) the catalyst surface was dominantly covered by NH$_3$ adsorbed species again. Therefore, it can be concluded that the NH$_3$-SCR reaction over this 5% WO$_x$/Fe$_2$O$_3$ catalyst mainly proceeded through an E-R reaction pathway during which the gaseous NO could directly react with active NH$_3$ adsorbed species, and this was also the main reason for its high SO$_2$ durability because NO$_x$ did not need to adsorbed onto the catalyst surface competitively as nitrates or nitrites.

4. Conclusions

Using conventional impregnation method, a series of δ% WO$_x$/Fe$_2$O$_3$ catalysts (δ = 1, 5, 10 by weight) were prepared, among which 5% WO$_x$/Fe$_2$O$_3$ catalyst showed the highest NH$_3$-SCR performance and excellent N$_2$ selectivity plus SO$_2$ resistance. The bulk structure of Fe$_2$O$_3$ was not influenced by WO$_x$ deposition, and the WO$_x$ species in highly unsaturated coordination state mainly acted as an effective surface modifier. This simple surface modification process increased the oxidation ability of surface Fe$^{(3+\delta)+}$ species through electronic inductive effect in W−O−Fe bonds, suppressed the over-oxidation of NH$_3$ on bulk Fe$_2$O$_3$ to enhance the N$_2$ selectivity, and supplied abundant surface reactive Lewis and Brønsted acid sites for NH$_3$ adsorption and thus resulted in easy activation of adsorbed NH$_3$ species on neighboring surface Fe$^{(3+\delta)+}$ sites with enhanced oxidation ability. Based on the detailed *in situ* DRIFTS study, the E-R reaction pathway between gaseous NO and active NH$_3$ adsorbed species was dominant over this WO$_x$ promoted Fe$_2$O$_3$ catalyst, which was the main reason for its high SO$_2$ durability. The surface modification of Fe$_2$O$_3$ by WO$_x$ deposition is an efficient way to improve the NH$_3$-SCR activity and N$_2$ selectivity through the tuning of redox ability and surface acidity simultaneously, which may also be applicable to other materials (V$_2$O$_5$, Cr$_2$O$_3$, MnO$_x$, CuO, CeO$_2$, Nb$_2$O$_5$ *etc.*) in the deNO$_x$ area.

2017YFC0211105, and 2017YFC0212502), the Key Project of National Natural Science Foundation of China (21637005), and the Photon Factory, IMSS-KEK, Japan (Project No. 2012G537).

Appendix A. Supplementary data

Supplementary material related to this article can be found, in the online version, at doi:https://doi.org/10.1016/j.apcatb.2018.02.052.

References

[1] V.I. Pavulescu, P. Grange, B. Delmon, Catal. Today 46 (1998) 233.
[2] Z. Liu, S. Ihl Woo, Catal. Rev. 48 (2006) 43.
[3] G. Busca, L. Lietti, G. Ramis, F. Berti, Appl. Catal. B 18 (1998) 1.
[4] M. Koebel, M. Elsener, M. Kleemann, Catal. Today 59 (2000) 335.
[5] W. Shan, H. Song, Catal. Sci. Technol. 5 (2015) 4280.
[6] F. Liu, Y. Yu, H. He, Chem. Commun. 50 (2014) 8445.
[7] K.J. Lee, P.A. Kumar, M.S. Maqbool, K.N. Rao, K.H. Song, H.P. Ha, Appl. Catal. B 142–143 (2013) 705.
[8] P. Granger, V.I. Parvulescu, Chem. Rev. 111 (2011) 3155.
[9] R.Q. Long, R.T. Yang, J. Am. Chem. Soc. 121 (1999) 5595.
[10] J.H. Kwak, R.G. Tonkyn, D.H. Kim, J. Szanyi, C.H.F. Peden, J. Catal. 275 (2010) 187.
[11] L. Ren, L. Zhu, C. Yang, Y. Chen, Q. Sun, H. Zhang, C. Li, F. Nawaz, X. Meng, F.-S. Xiao, Chem. Commun. 47 (2011) 9789.
[12] W. Shan, F. Liu, Y. Yu, H. He, C. Deng, X. Zi, Catal. Commun. 59 (2015) 226.
[13] Y. Peng, J. Li, L. Chen, J. Chen, J. Han, H. Zhang, W. Han, Environ. Sci. Technol. 46 (2012) 2864.
[14] W. Shan, F. Liu, Y. Yu, H. He, Chin. J. Catal. 35 (2014) 1251.
[15] P. Li, Y. Xin, Q. Li, Z. Wang, Z. Zhang, L. Zheng, Environ. Sci. Technol. 46 (2012) 9600.
[16] X. Mou, B. Zhang, Y. Li, L. Yao, X. Wei, D.S. Su, W. Shen, Angew. Chem. Int. Ed. 51 (2012) 2989.
[17] N. Apostolescu, B. Geiger, K. Hizbullah, M.T. Jan, S. Kureti, D. Reichert, F. Schott, W. Weisweiler, Appl. Catal. B 62 (2006) 104.
[18] F. Liu, H. He, C. Zhang, Chem. Commun. (2008) 2043.
[19] J.P. Chen, M.C. Hausladen, R.T. Yang, J. Catal. 151 (1995) 135.
[20] S. Yang, J. Li, C. Wang, J. Chen, L. Ma, H. Chang, L. Chen, Y. Peng, N. Yan, Appl. Catal. B 117–118 (2012) 73.
[21] P. Fabrizioli, T. Bürgi, A. Baiker, J. Catal. 206 (2002) 143.
[22] H. Teng, L.-Y. Hsu, Y.-C. Lai, Environ. Sci. Technol. 35 (2001) 2369.
[23] G. Marbán, A.B. Fuertes, Catal. Lett. 84 (2002) 13.
[24] L. Chen, J. Li, W. Ablikim, J. Wang, H. Chang, L. Ma, J. Xu, M. Ge, H. Arandiyan, Catal. Lett. 141 (2011) 1859.
[25] W. Shan, F. Liu, H. He, X. Shi, C. Zhang, Chem. Commun. 47 (2011) 8046.
[26] B.A. Kolesov, C.A. Geiger, Am. Mineral. 91 (2006) 1039.
[27] F. Liu, H. He, Catal. Today 153 (2010) 70.
[28] J.W. Cook, D.E. Sayers, J. Appl. Phys. 52 (1981) 5024.
[29] A.L. Ankudinov, B. Ravel, J.J. Rehr, S.D. Conradson, Phys. Rev. B 58 (1998) 7565.
[30] S. Yamazoe, Y. Hitomi, T. Shishido, T. Tanaka, J. Phys. Chem. C 112 (2008) 6869.
[31] F. Liu, H. He, C. Zhang, Z. Feng, L. Zheng, Y. Xie, T. Hu, Appl. Catal. B 96 (2010) 408.
[32] F. Liu, K. Asakura, P. Xie, J. Wang, H. He, Catal. Today 201 (2013) 131.
[33] F. Liu, H. He, Z. Lian, W. Shan, L. Xie, K. Asakura, W. Yang, H. Deng, J. Catal. 307 (2013) 340.
[34] J. Fang, X. Bi, D. Si, Z. Jiang, W. Huang, Appl. Surf. Sci. 253 (2007) 8952.
[35] X. Li, X. Li, J. Li, J. Hao, Chem. Eng. J. 317 (2017) 70.
[36] Z. Liu, Y. Liu, Y. Li, H. Su, L. Ma, Chem. Eng. J. 283 (2016) 1044.
[37] Z. Feng, C.-Y. Kim, J.W. Elam, Q. Ma, Z. Zhang, M.J. Bedzyk, J. Am. Chem. Soc. 131 (2009) 18200.
[38] L.J. France, Q. Yang, W. Li, Z. Chen, J. Guang, D. Guo, L. Wang, X. Li, Appl. Catal. B 206 (2017) 203.
[39] S. Shwan, J. Jansson, L. Olsson, M. Skoglundh, Appl. Catal. B 166–167 (2015) 277.
[40] J. Cao, Y. Wang, X. Yu, S. Wang, S. Wu, Z. Yuan, Appl. Catal. B 79 (2008) 26.
[41] M. Liang, W. Kang, K. Xie, J. Nat. Gas Chem. 18 (2009) 110.
[42] W. Qian, Y. Su, X. Yang, M. Yuan, W. Deng, B. Zhao, J. Fuel Chem. Technol. 45 (2017) 1499.
[43] S. Brandenberger, O. Kröcher, A. Tissler, R. Althoff, Appl. Catal. B 95 (2010) 348.
[44] M. Høj, M.J. Beier, J.-D. Grunwaldt, S. Dahl, Appl. Catal. B 93 (2009) 166.
[45] M. Schwidder, M. Santhosh Kumar, A. Bruckner, W. Grunert, Chem. Commun. (2005) 805.
[46] M. Devadas, O. Kröcher, M. Elsener, A. Wokaun, G. Mitrikas, N. Söger, M. Pfeifer, Y. Demel, L. Mussmann, Catal. Today 119 (2007) 137.
[47] X.-R. Chen, C.-L. Chen, N.-P. Xu, C.-Y. Mou, Catal. Today 93–95 (129) (2004).
[48] Q. Zhao, S.-L. Chen, J. Gao, C. Xu, Transit. Metal Chem. 34 (2009) 621.
[49] G. Ramis, L. Yi, G. Busca, Catal. Today 28 (1996) 373.
[50] L. Ma, J. Li, R. Ke, L. Fu, J. Phys. Chem. C 115 (2011) 7603.
[51] L. Chen, J. Li, M. Ge, Environ. Sci. Technol. 44 (2010) 9590.
[52] Z. Wu, B. Jiang, Y. Liu, H. Wang, R. Jin, Environ. Sci. Technol. 41 (2007) 5812.
[53] R.Q. Long, R.T. Yang, J. Catal. 186 (1999) 254.
[54] G. Ramis, M.A. Larrubia, G. Busca, Top. Catal. 11 (2000) 161.
[55] Z. Si, D. Weng, X. Wu, J. Li, G. Li, J. Catal. 271 (2010) 43.
[56] H.-H. Zhao, G.-Y. Xie, Z.-Y. Liu, Y.-Z. Liu, Acta Chim. Sinica 66 (2008) 1021.
[57] J.G. Amores, V.S. Escribano, G. Ramis, G. Busca, Appl. Catal. B 13 (1997) 45.
[58] G. Ramis, L. Yi, G. Busca, M. Turco, E. Kotur, R.J. Willey, J. Catal. 157 (1995) 523.
[59] K. Suzuki, T. Noda, N. Katada, M. Niwa, J. Catal. 250 (2007) 151.
[60] K. Suzuki, Y. Aoyagi, N. Katada, M. Choi, R. Ryoo, M. Niwa, Catal. Today 132 (2008) 38.
[61] T. Noda, K. Suzuki, N. Katada, M. Niwa, J. Catal. 259 (2008) 203.
[62] K. Suzuki, N. Katada, M. Niwa, J. Phys. Chem. C 111 (2007) 894.
[63] K. Suzuki, G. Sastre, N. Katada, M. Niwa, Phys. Chem. Chem. Phys. 9 (2007) 5980.
[64] F. Lónyi, J. Valyon, Microporous Mesoporous Mater. 47 (2001) 293.
[65] W.L. Earl, P.O. Fritz, A.A.V. Gibson, J.H. Lunsford, J. Phys. Chem. 91 (1987) 2091.
[66] N.-Y. Topsøe, Science 265 (1994) 1217.
[67] M.A. Larrubia, G. Ramis, G. Busca, Appl. Catal. B 30 (2001) 101.
[68] L. Chen, J. Li, M. Ge, L. Ma, H. Chang, Chin. J. Catal. 32 (2011) 836.
[69] W.S. Kijlstra, D.S. Brands, H.I. Smit, E.K. Poels, A. Bliek, J. Catal. 171 (1997) 219.
[70] F. Liu, H. He, C. Zhang, W. Shan, X. Shi, Catal. Today 175 (2011) 18.
[71] J.D. Russell, Clay Miner. 14 (1979) 109.
[72] Z. Liu, P.J. Millington, J.E. Bailie, R.R. Rajaram, J.A. Anderson, Microporous Mesoporous Mater. 104 (2007) 159.
[73] W.S. Kijlstra, D.S. Brands, E.K. Poels, A. Bliek, J. Catal. 171 (1997) 208.
[74] G.M. Underwood, T.M. Miller, V.H. Grassian, J. Phys. Chem. A 103 (1999) 6184.
[75] A. Martinez-Arias, J. Soria, J.C. Conesa, X.L. Seoane, A. Arcoya, R. Cataluna, J. Chem. Soc. Faraday Trans. 91 (1995) 1679.
[76] K.I. Hadjiivanov, Catal. Rev. 42 (2000) 71.
[77] G. Qi, R.T. Yang, R. Chang, Appl. Catal. B 51 (2004) 93.
[78] G. Piazzesi, M. Elsener, O. Krocher, A. Wokaun, Appl. Catal. B 65 (2006) 169.
[79] W. Xu, C.T. Johnston, P. Parker, S.F. Agnew, Clays Clay Miner. 48 (2000) 120.
[80] R.L. Frost, Spectrochim. Acta A 60 (2004) 1469.
[81] A. Hodgson, S. Haq, Surf. Sci. Rep. 64 (2009) 381.
[82] A. Destainville, E. Champion, D. Bernache-Assollant, E. Laborde, Mater. Chem. Phys. 80 (2003) 269.
[83] F. Liu, W. Shan, Z. Lian, L. Xie, W. Yang, H. He, Catal. Sci. Technol. 3 (2013) 2699.